metals

MDPI

Article

Investigation of Mechanical Properties and Wear Resistance of A2/B2 Type Medium-Entropy Alloy Matrix Reinforced with Tungsten Particles by In-Situ Reaction

Mingyu Wu [1], Guijiang Diao [1], Zhen Xu [1], Ruiken Sim [1], Wengang Chen [2], Daolun Chen [3] and Dongyang Li [1,*]

[1] The Department of Chemical and Materials Engineering, University of Alberta, Edmonton, AB T6G 2H5, Canada
[2] College of Mechanical & Transportation Engineering, Southwest Forest University, Kunming 650224, China
[3] Department of Mechanical and Industrial Engineering, Toronto Metropolitan University, Toronto, ON M5B 2K3, Canada
* Correspondence: dongyang.li@ualberta.ca

Abstract: Microstructure, mechanical properties, wear resistance, corrosion and corrosive wear resistance of $AlCrFeNiW_x$ (x = 0, 0.1, 0.2, 0.3 and 0.4) medium-entropy alloys (MEAs) prepared by vacuum arc melting process were investigated. Results of the study show that the microstructure of as-cast $AlCrFeNiW_x$ alloys is composed of one disordered Fe-Cr rich BCC phase (A2) and one ordered NiAl-rich (B2) phase when x = 0 and 0.1; W particles appear when $x \geq 0.2$. Hardness and strength of AlCrFeNi alloy are markedly increased by the W addition. The strengthening mechanisms include solid-solution strengthening, nano-sized precipitation strengthening and second phase strengthening. The excellent ductility of AlCrFeNi is retained with minor W addition ($x \leq 0.2$) but it considerably declines as more W is added, resulting from the precipitation of excessive large-sized W particles. W addition improves the pitting resistance and passivation property of AlCrFeNi HEA in 3.5 wt. % NaCl solution. It is shown that $AlCrFeNiW_{0.3}$ possesses the highest corrosion resistance, as reflected by the highest E_{corr} and the lowest I_{corr}. Tungsten notably enhances the resistance of this HEA to wear and corrosive wear. $AlCrFeNiW_{0.4}$ with the highest strength and hardness exhibits the lowest wear volume loss under both dry and corrosive wear conditions.

Keywords: AlCrFeNi HEA; W addition; microstructure; wear; corrosive wear

Citation: Wu, M.; Diao, G.; Xu, Z.; Sim, R.; Chen, W.; Chen, D.; Li, D. Investigation of Mechanical Properties and Wear Resistance of A2/B2 Type Medium-Entropy Alloy Matrix Reinforced with Tungsten Particles by In-Situ Reaction. *Metals* **2023**, *13*, 656. https://doi.org/10.3390/met13040656

Academic Editor: Jiro Kitagawa

Received: 17 February 2023
Revised: 20 March 2023
Accepted: 23 March 2023
Published: 25 March 2023

1. Introduction

High-entropy alloys (HEAs), medium-entropy alloys (MEAs) or multi-principal component alloys (MCAs) have attracted considerable interest, which consist of more than four principal elements with nearly equimolar ratios. In HEAs and MEAs, the simple solid-solution structures such as face-centered cubic (FCC) structure, body-centered cubic (BCC) structure, or hexagonal closed-packed (HCP) structure are inclined to form due to their higher entropy of mixing the multi-elements [1–5]. The HEAs and MEAs more or less avoid the drawbacks of conventional alloys and profit from the mutual interaction of various elements and lattice distortion, showing various wish-for capabilities such as well-balanced strength and ductility, superior performance at high and low temperatures, good corrosion and wear resistance [6–13]. The equiatomic CrFeCoNi and CrFeCoNiMn alloys, as the earliest studied HEAs, still attract marked attention because of their single FCC phase structure which remains stable even aged in a wide range of temperatures [14–18]. Although possessing excellent ductility, the comparatively low strength and hardness of FCC-type HEAs restrict their applications [14,19,20]. For example, CrFeCoNi exhibits high ductility (more than 75%) but low yield strength (190 MPa) at room temperature [21]. Adding alloying elements (V, Ti, Y, Nb, Zr, Ta, Hf and W) to the FCC-typed HEA, e.g., CrFeCoNi and CuFeCoNi, is a common method to improve their mechanical strength [21–29]. However,

the increase of strength is limited and the appearance of hard and brittle intermetallic phases could severely sacrifice the inherent ductility of the HEA matrix.

The BCC structure is generally harder or stronger than the FCC structure, due to its higher energy barriers for the edge dislocation motion, at the expense of ductility [30,31]. It is recently reported that the coherent precipitated ordered BCC (B2) phase into disordered BCC (A2) matrix has great potential for improving the strength and toughness [32–34]. Since Al has the strong bonding with transition metals Fe and Ni, Al-containing B2 structured high-entropy solid solutions could be achieved in multi-principal component alloys. It has been found that the microstructure of $Al_xCrFeNi$ alloy could completely transform into FeCr-rich A2 and NiAl-rich B2 when $x \geq 0.4$ [35,36]. Jiang et al. [37] showed that the AlCrFeNi alloy which was obtained by the cold crucible levitation melting (CCLM) process exhibited the combinations of relatively high yield strength of 1075 MPa and fairly high fracture strain of 43.8%, attributing to the assembly of A2 and B2 lamellar eutectic microstructure and the solid solution strengthening derived from the Al atoms in the MEA matrix. Actually, five-component AlCrFeCoNi alloy is commonly used in many studies on A2/B2 structures. In the previous research, it was found that there is little difference in the Co content between the A2 and B2 phases for AlCrFeCoNi alloy which exhibited similar hardness and strength with those of AlCrFeNi. More importantly, the Co-containing alloy showed significantly worse toughness and wear resistance than Co-free one [38–42]. Given the high cost of Co and the focus of this research on wear resistance, in this present study the AlCrFeNi MEA was selected as a reference material to investigate the effect of adding alloying elements on the mechanical and wear resistance of A2/B2-structured alloy.

Tungsten as a refectory element with a large atomic size (0.1367 nm) and high Young's modulus (411 GPa), is considered as a good reinforcement in the form of second phase. The tungsten particle-reinforced Zr-based and Al-based alloys have been reported for improving strength and plasticity [43,44]. Mazilkin et al. [45] noticed that the W particles distribute homogeneously in Fe-Cr alloy with added W, leading to the formation of finer but more elongated grains. The W-added Fe-Cr alloy exhibits better mechanical properties, in terms of both strength and plasticity. Besides, W can cause severe lattice distortion when it dissolves into the alloys, thus giving rise to effective solid solution strengthening [27,46–48]. It is therefore expected that adding W to the Co-free AlCrFeNi alloy under study may lead to a good balance between strength and ductility. Up to date, there are few detailed studies about the effect of W on the microstructure and properties of BCC-structured HEA or MEA, especially on the wear and corrosion resistance. In the present work, W-added A2/B2-type AlCrFeNi MEAs were studied, which were prepared by cold-mold arc melting method. The microstructure, mechanical properties, dry wear resistance, corrosion and corrosive resistance in the 3.5 wt. % NaCl solution for $AlCrFeNiW_x$ (x = 0, 0.1, 0.2, 0.3 and 0.4) MEAs were investigated in detail.

2. Experimental Procedure

Ingots of five $AlCrFeNiW_x$ MEAs with different molar ratios of tungsten (x = 0, 0.1, 0.2, 0.3 and 0.4, named W0, W1, W2, W3 and W4, respectively) were prepared by arc melting metal powders (purity $\geq$ 99.5 at. %) in a water-cooled copper crucible in a high-purity argon atmosphere. The process of flipping, melting and solidifying each ingot was repeated at least four times to improve the compositional homogeneity. Samples having dimensions of $10 \times 10 \times 4$ mm^3 were cut from the alloy ingots by wire electrical discharge machining (WEDM), and subsequently ground with SiC papers up to 1200 grits, and finally polished using a 0.1 μm alumina suspension.

The phase analysis of X-ray diffraction was conducted for the $AlCrFeNiW_x$ MEA samples using a Bruker D8 Discover instrument (Bruker Ltd., Coventry, UK) with Cu Kα radiation (λ = 0.15418 Å) having 2θ ranging from 20 to 90° at a scanning rate of 4° min^{-1}. The microstructural and compositional analyses of the $AlCrFeNiW_x$ MEA samples were carried out using a scanning electron microscope (SEM, Sigma 300 VP-FESEM, Zeiss, Oberkochen, German) equipped with an energy dispersive spectrometer (EDS).

Nanoindentation tests were performed on selected regions of the polished sample surface using an NHT3 nanoindenter (Anton Paar, Saint-Laurent, QC, Canada) with a three-sided Berkovich-type tip. The dynamic load with a maximum value of 200 mN was applied for each indention test, during which the load ~ the penetration depth curve was recorded. The loading-unloading rate was 3 mN/s and the dwell time was 10 s. The spacing between each 2 neighboring indentation points was at least 10 μm. Vickers hardness was measured using a Vickers hardness tester (MH-5L) under a load of 500 g for 5 s. At least seven measurements were made for each specimen to determine the average hardness. Cylindrical specimens with dimensions of ϕ 4 × 7.5 mm were cut from MEA ingots for compressive tests. The compressive test was performed using a 313 electromechanical universal test machine (TES-TRESOURCES, Shakopee, MN, USA) at a displacement of 0.3 mm/min. At least three repeated compressive tests were performed for each alloy.

The Gamry PC4/759 (Gamry, Warminster, US) electrochemical workstation was used to investigate the corrosion resistance of $AlCrFeNiW_x$ in 3.5 wt. % NaCl solution. The MEA samples with an exposing area of 1 cm^2 acted as the working electrode. The platinum plate and saturated calomel electrode (SCE) were selected as the counter electrode and reference electrode, respectively. Before the polarization test, the samples were held at the open circuit condition for 60 min to achieve a steady state. The polarization measurements were conducted with the scan speed of 0.5 mV/s for potential ranging from –0.4 V_{SCE} vs. OCP to 1.2 V_{SCE}, or manually stopped when pitting corrosion occurred and the current density excessed 10^{-4} A/cm^2.

The wear tests were performed in the dry condition and corrosive environment, respectively, using a pin-on-disc wear testing machine (CSEM Tribometer, Peseux, Switzerland) under a normal load of 10 N. Two wear tests were conducted to evaluate the performance of the alloys under dry wear conditions. The first was conducted without any air flow, while the second was conducted with an air flow to cool the sample surface which was done to minimize the oxidation caused by the frictional heat during the test. For the corrosive wear test, the sample was completely immersed in the 3.5 wt. % NaCl solution. The sliding velocity and distance were 2 cm/s and 45 m, respectively. The circular path was 2.4 mm in diameter. The counterpart was a Si_3N_4 ball with a diameter of 3 mm. For each test, a fresh surface of Si_3N_4 ball was used to make sure that the system work under the same condition. After the wear test, volume losses of samples were determined based on the dimensions of wear tracks using a 3D optical profilometer (ZeGage, Middlefield, CT, USA). The reported value of volume loss for each sample is an average of results over three repeated tests. Morphologies of wear track and composition of wear debris were further examined using SEM equipped with EDS.

3. Results

3.1. Phase Characterization

The XRD patterns of as-cast $AlCrFeNiW_x$ MEAs are presented in Figure 1. Two BCC domains are observed in AlCrFeNi, which are characterized as a FeCr-rich disordered BCC phase (A2) and a NiAl-rich ordered BCC phase (B2), respectively. Due to the similar lattice constants, the diffraction peaks of (110), (200) and (211) crystal planes of A2 and B2 phases coincide with each other while B2 phase has a unique (100) crystal plane which is around 31.5°. By using the equation of Bragg's law, the lattice parameters of A2 and B2 phase were determined to be 2.882 Å. With 0.1 molar ratio of added W, the diffraction pattern of the alloy remains the same, indicating that the crystal structure still consists of A2 and B2 phases. The incorporated W completely is dissolved in the present phases. For $AlCrFeNiW_x$ (x = 0.2–0.4) alloys, diffraction peaks corresponding to W (BCC structure, ICSD Card no. 1-1203) emerge in the XRD patterns and their intensity is gradually enhanced with increasing W content. The phase identification closely matches that found in the reported literature [27].

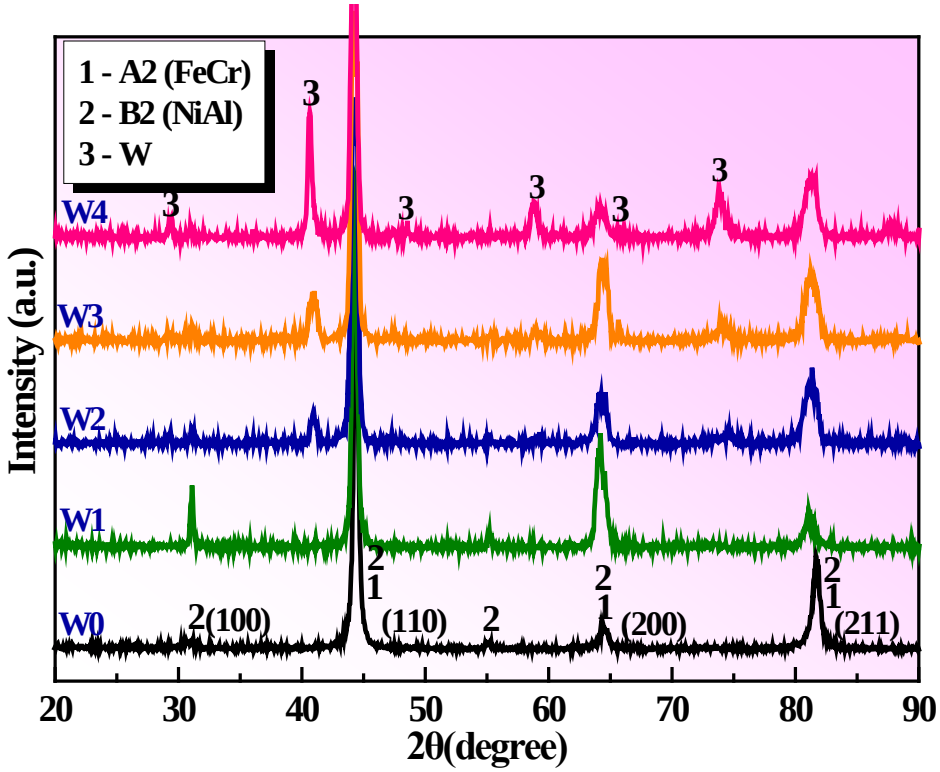

Figure 1. X-ray diffraction patterns of AlCrFeNi, AlCrFeNi$W_{0.1}$, AlCrFeNi$W_{0.2}$, AlCrFeNi$W_{0.3}$ and AlCrFeNi$W_{0.4}$ MEAs.

3.2. Phase Formation Prediction

Phase prediction in HEAs or MEAs has been a burdensome task not only for fundamental understanding but for various applications which require promoting some phases and suppressing others that could negatively affect properties of the alloys. Various models for thermodynamic parameters, such as the mixing enthalpy (ΔH_{mix}), mixing entropy (ΔS_{mix}), atomic size difference (δ), solid solution parameter (Ω), valence electron concentration (VEC), geometrical parameter (Λ), are empirically or semi-empirically suggested to predict the phase formation and stability in the multi-component alloys [49–53]. These parameters are expressed by the following equations:

$$\Delta H_{mix} = \sum_{i=1, i\neq j}^{n} 4\Delta H_{AB}^{mix} c_i c_j \quad (1)$$

$$\delta = \sqrt{\sum_{i=1}^{n} c_i \left(1 - \frac{r_i}{r}\right)^2} \quad (2)$$

$$\Delta S_{mix} = -R\sum_{i=1}^{n} (c_i ln c_i) \quad (3)$$

$$r = \sum_{i=1}^{n} c_i r_i \quad (4)$$

$$\Omega = \frac{T_m \Delta S_{mix}}{|\Delta H_{mix}|} \quad (5)$$

$$\Lambda = \Delta S_{mix} / \delta^2 \quad (6)$$

$$VEC = \sum_{i=1}^{n} c_i (VEC)_i \quad (7)$$

where ΔH_{AB}^{mix} stands for the mixing enthalpy of elements A and B; c_i and r_i are the atomic percent and atomic radius of the ith element, respectively; $r = \sum_{i=1}^{n} c_i r_i$ is the average atomic radius; R the gas constant (8.314 $Jmol^{-1}K^{-1}$); $T_m = \sum_{i=1}^{n} c_i (T_m)_i$, where $(T_m)_i$ is the melting point of the ith element. $(VEC)_i$ is the VEC value of the ith element. The mixing enthalpy for binary atomic pairs, atomic radius and VEC of each element in the studied HEA system are listed in Table 1. Calculated parameters ΔS_{mix}, ΔH_{mix}, δ, Ω, Λ and VEC for the studied alloys are listed in Table 2.

Table 1. The mixing enthalpy of binary atomic pairs and physiochemical parameters of constituent elements.

Elements	Enthalpy of Mixing (KJ/mol)					VEC_i	Atomic Radius (Å)
	Al	Cr	Fe	Ni	W		
Al	0					3	1.432
Cr	−10	0				6	1.249
Fe	−11	−1	0			8	1.241
Ni	−22	−7	−2	0		10	1.246
W	−2	1	0	−3	0	6	1.367

Table 2. Calculated parameters of $AlCrFeNiW_x$ (x = 0, 0.1, 0.2, 0.3 and 0.4) MEAs.

MEAs	ΔH_{mix}(kJ/mol)	δ (%)	VEC	ΔS_{mix}(J/mol/K)	Ω	Λ
W0	−13.25	6.26	6.75	11.53	1.43	0.29
W1	−12.71	6.24	6.73	12.19	1.63	0.31
W2	−12.19	6.22	6.71	12.57	1.8	0.32
W3	−11.72	6.19	6.69	12.83	1.96	0.33
W4	−11.28	6.17	6.68	13.01	2.11	0.34

The parameters ΔS_{mix}, ΔH_{mix}, δ, Ω are indicators for the stability of the solid solution phase. Zhang et al. [49] proposed that the solid solution would be stable when ΔS_{mix}, ΔH_{mix}, δ were in the regions of $12 \leq \Delta S_{mix} \leq 17.5$ J/mol, $-15 < \Delta H_{mix} < 5$ kJ/mol and $\delta \leq 6.6\%$, respectively. The values of ΔH_{mix} and δ for $AlCrFeNiW_x$ (x = 0, 0.1, 0.2, 0.3 and 0.4) under study are $11.53 \leq \Delta S_{mix} \leq 13.01$ J/mol, $-13.25 \leq \Delta H_{mix} \leq -11.28$ kJ/mol and $6.17\% \leq \delta \leq 6.26\%$, which are in the range of forming a solid solution. A new parameter Ω, which combines the effect of ΔS_{mix} and ΔH_{mix}, was introduced [51] to determine the formation of solid solution phase. The study indicated that the formation of stable solid solution would occur when $\Omega \geq 1.1$. The values of Ω for the MEA samples in the present study are in the range of $1.42 \leq \Omega \leq 2.11$, which fall into the required region of Ω for phase stability. It has been known from XRD results that all the studied MEAs exhibit a combined solid solution structure, suggesting that ΔH_{mix}, δ and Ω successfully predicted the phase formation for the $AlCrFeNiW_x$ system.

The stability of FCC or BCC solid solution phase would be determined by the physical parameter VEC which was proposed by Guo et al. [50]. The calculated values of VEC for the $AlCrFeNiW_x$ (x = 0, 0.1, 0.2, 0.3 and 0.4) are $6.68 \leq VEC \leq 6.75$ (Table 2), which are in the region favoring the formation of stable BCC phase (VEC < 6.87). This argument is in agreement with the XRD results indicating the formation of BCC duplex or triple phases in the alloys under study (Figure 1). Besides, Singh et al. [52] developed a geometrical parameter (Λ) and prescribed range of [0.24, 0.96] to predict the formation of disordered solid solution plus ordered solid solution/compounds. According to Table 2, the calculated Λ values for the MEAs under study fall into the required region of Λ for A2 and B2 phases. Overall, the phase compositions inferred from empirical parameters are in accord with the

experimental results. These parameters can be well combined to predict the precipitation behavior and determine the alloy composition in the studied MEAs.

3.3. Microstructure

Figure 2 shows SEM micrographs of AlCrFeNi and $AlCrFeNiW_{0.1}$ alloys. Magnified images are illustrated in Figure 2b–f. Chemical compositions of different regions in the AlCrFeNi and $AlCrFeNiW_{0.1}$ alloys are listed in Table 3. The microstructure of the AlCrFeNi alloy consists of the dark-bright rod alternating weave spinodal decomposition intragranular structure and the lamellar eutectic structure sitting at the grain boundary (Figure 2a,b). According to the EDS and XRD results, the well-marked bright and dark domains are Fe-Cr-rich A2 phase and NiAl-rich B2 phase, respectively. The two characteristic structures are both the mixture of A2 and B2 phases. Different from the phase formation through "nucleation and growth", spinodal decomposition is a spontaneous reaction by which a homogenous, supersaturated single phase separates into two coexisting phases [54,55] through uphill diffusion to achieve the free energy minimum. They have characteristic intertwined structures and grow into compositional modulations (each of them is rich in one component and poor in the other).

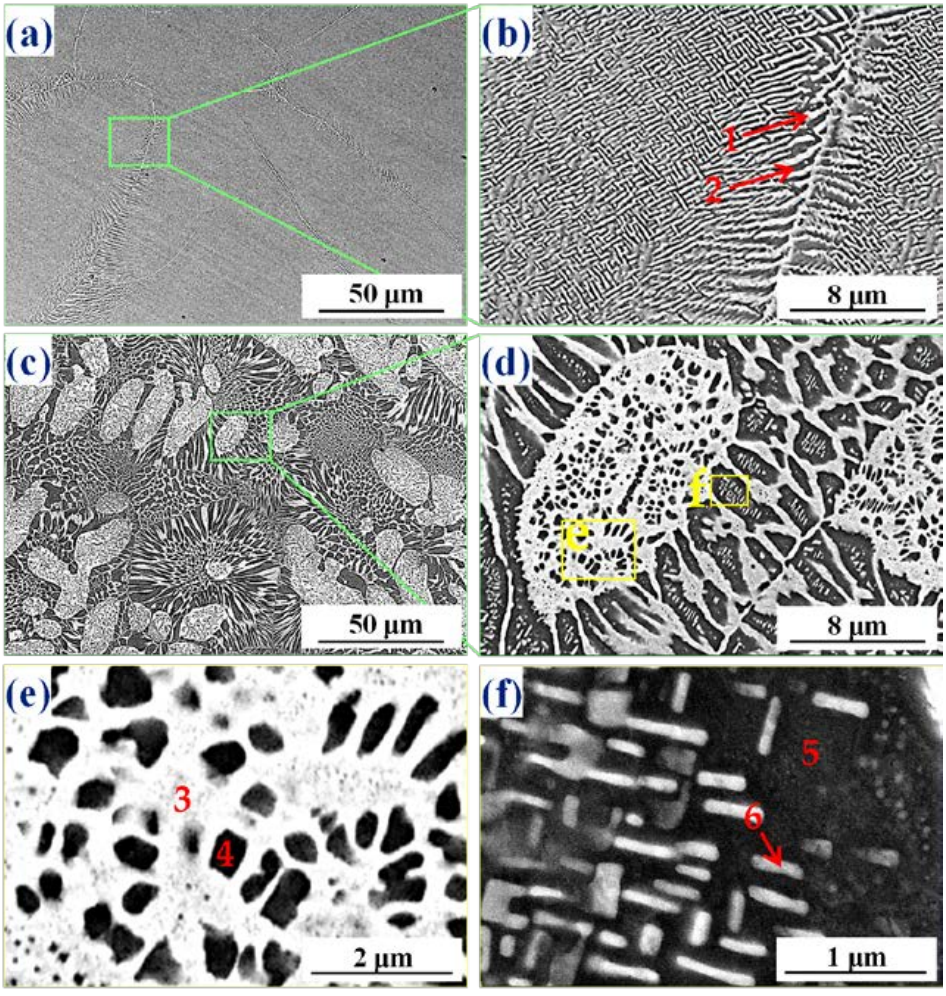

Figure 2. SEM backscattered electron micrographs of (**a**,**b**) AlCrFeNi, (**c**–**f**) $AlCrFeNiW_{0.1}$ MEAs. Images (**b**,**d**) are high-magnification views of green squares in image (**a**,**c**). Images (**e**,**f**) are the enlarged view on the nanoscale of yellow squares (marked with "e" and "f") in image (**d**).

Table 3. Compositions (at. %) of different regions for $AlCrFeNiW_x$ (x = 0 and 0.1) alloys.

Alloys	Areas	Al	Cr	Fe	Ni	W
AlCrFeNi	1	17.3	38.6	33.8	10.3	
	2	38.2	13.0	15.2	33.7	
$AlCrFeNiW_{0.1}$	3	9.1	43.5	36.6	6.6	4.2
	4	12.5	36.1	34.1	15.7	1.7
	5	32.5	15.1	18.3	33.6	0.5
	6	30.5	17.3	20.2	30.8	1.3

The microstructure completely changed with incorporation of minor W into the AlCrFeNi alloy (Figure 2c,d). As can be seen, considerable amounts of block regions and the surrounding flower-like eutectic microstructure appear in $AlCrFeNiW_{0.1}$ alloy. In particular, a few precipitates at the nano-scale are observed to form in the block region and dark domain of the eutectic microstructure, marked by "E" and "F" respectively (Figure 2d). An enlarged view of the precipitate morphology is presented in Figure 2e,f. Additional study of the microstructure using SEM-EDS indicates that the block regions are enriched in Fe, Cr and W, and the nano-precipitates have lower content of W making them darker in contrast (Figure 2e).

The opposite of contrast is observed for the eutectic microstructure, in which the nano-precipitates are brighter, exhibiting the higher W content than the surrounding dark parent body (Figure 2f). Because of its relatively large size and limited solid solubility, the element W can cause fluctuations in composition between the nanoprecipitates and the matrix. This is necessary to maintain similar lattice constants between the two separated phases with the same crystal structure. By doing so, the interface energy is reduced [56,57]. In general, W mostly stays as a solid solute in A2 phase, and depletes in B2 phase. As shown in Table 1, W-Ni and W-Al pairs have much lower negative enthalpy of mixing, compared with the Ni-Al pair in B2 phase. This indicates that W is unlikely the core element to promote the stability of B2 phase. Therefore, W is preferred to dissolve in Ni/Al-depleted disordered BCC phase (A2), which appears brighter in the BSE mode.

The SEM microstructure images of AlCrFeNi MEA reinforced by W with molar ratios in the range of 0.2–0.4 are shown in Figure 3. Chemical compositions of different regions in the $AlCrFeNiW_x$ ($0.2 \leq x \leq 0.4$) alloys are listed in Table 4. The block regions and flower-like eutectic structure similar to those of $AlCrFeNiW_{0.1}$ are prevalent in all the alloys. Moreover, the presence of bright particles having increasing size and amounts with increasing W is observed in $AlCrFeNiW_x$ ($x \geq 0.2$). The bright particles are found to contain more than 80 at. % W with a small amount of other elements. Combining EDS analysis for points and map with the XRD results, it is confirmed that W particles appeared in $AlCrFeNiW_x$ when $x \geq 0.2$ though they contained minor other elements, whose contents decreased as x continuously increased, indicating that the solid solubility of W in Fe-Cr rich A2 phase is limited due to its larger atomic radius and its slightly negative or positive mixing enthalpy when being mixed with other four constituent elements.

Table 4. Compositions (at. %) of different regions for $AlCrFeNiW_x$ (x = 0.2, 0.3 and 0.4) alloys.

Alloys	Areas	Al	Cr	Fe	Ni	W
$AlCrFeNiW_{0.2}$	1	15.2	37.0	30.1	12.8	4.9
	2	33.7	14.8	18.4	32.3	0.9
	3	2.6	18.6	5.7	2.7	70.4
$AlCrFeNiW_{0.3}$	4	14.9	35.9	30.9	13.3	4.9
	5	41.6	8.7	13.1	36.0	0.5
	6	3.9	19.7	3.2	2.4	70.8
$AlCrFeNiW_{0.4}$	7	11.4	39.0	34.6	10.3	4.8
	8	32.6	15.2	19.1	32.3	0.7
	9	2.9	8.9	3.6	1.2	83.4

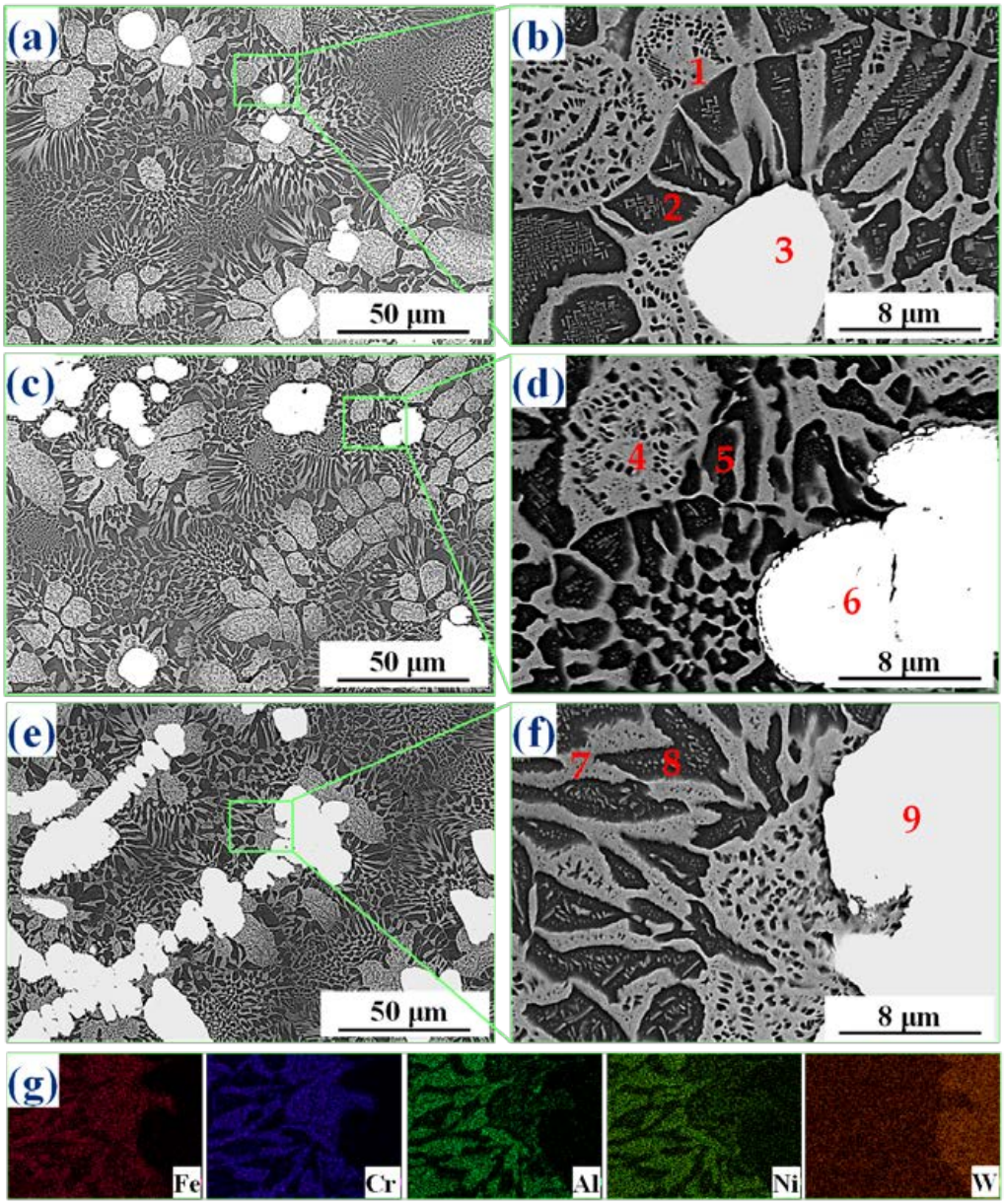

Figure 3. SEM backscattering electron micrographs of (**a**,**b**) $AlCrFeNiW_{0.2}$, (**c**,**d**) $AlCrFeNiW_{0.3}$ and (**e**,**f**) $AlCrFeNiW_{0.4}$ MEAs, respectively. Images (**b**,**d**,**f**) are high-magnification views of green squares in image (**a**,**c**,**e**). Image (**g**) is SEM/EDS elemental map of Fe, Cr, Al, Ni and W for image (**f**).

3.4. Mechanical Properties

Nano-indentation tests were conducted in selected regions to investigate the effect of W on micro-hardness of the local structure. Figure 4 displays SEM images with indentation locations and representative indentation load-displacement curves. The corresponding micro-hardness calculated using Oliver and Pharr Method and the overall hardness for the alloys are summarized and compared in Table 5.

As shown in Figure 4a, the microhardness measurements were carried out in the matrix regions for AlCrFeNi alloy, which cover a number of A2 + B2 domains. With 0.1 molar ratio of W addition, the indentation was made on additional block region (A2 phase). The solid solution of tungsten in A2 phase largely contributes to the increased local and bulk hardness values with minor tungsten addition. Similar results were reported in the literature [27], in which $(CoCuFeNi)_{95}W_5$ sample showed higher hardness than tungsten-free sample due to the solid solution of W in the Cu-depleted region of FCC phase.

In the present alloy system, nanometer-sized precipitation arising from the addition of minor W should also help to increase the hardness.

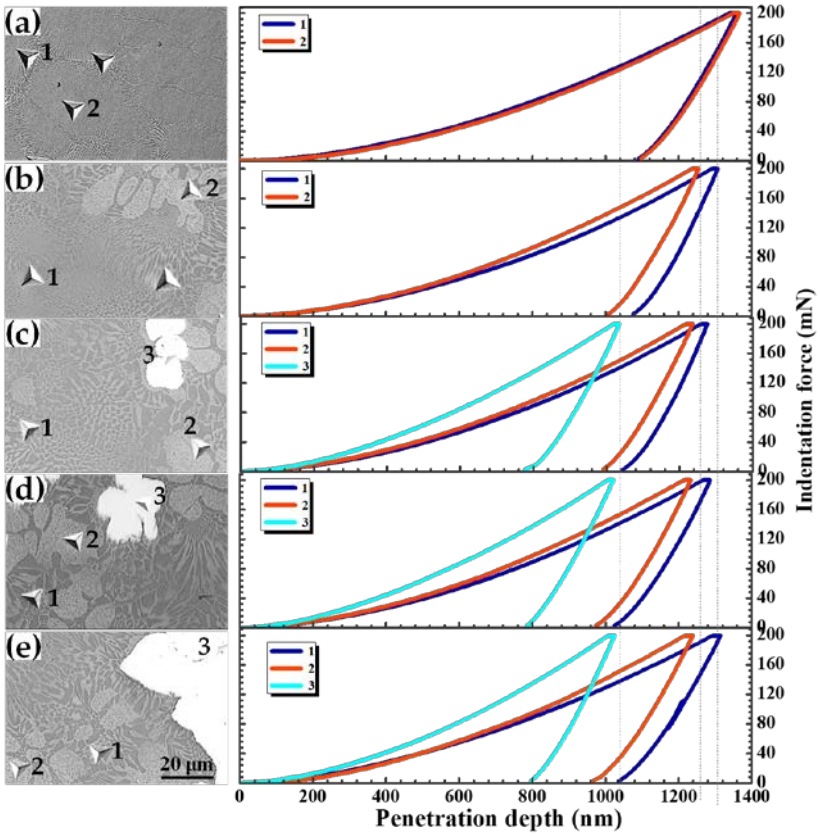

Figure 4. SEM images of representative indentations in different regions and the corresponding load-displacement curves for (**a**) AlCrFeNi, (**b**) AlCrFeNi$W_{0.1}$, (**c**) AlCrFeNi$W_{0.2}$, (**d**) AlCrFeNi$W_{0.3}$ and (**e**) AlCrFeNi$W_{0.4}$ samples.

Table 5. Specific regions micro-hardness and overall hardness of AlCrFeNiW_x MEAs.

Alloys	Regions	Micro-Hardness (MPa)	Overall Hardness (HV0.5)
AlCrFeNi	1 Matrix (BCC + B2)	5622.9	596.8
	2 Matrix (BCC + B2)	5633.8	
AlCrFeNi$W_{0.1}$	1 Matrix (BCC + B2)	6046.5	669.2
	2 Block BCC	6553.1	
AlCrFeNi$W_{0.2}$	1 Matrix (BCC + B2)	6185.5	736.9
	2 Block BCC	6889.8	
	3 W-particle	10,326	
AlCrFeNi$W_{0.3}$	1 Matrix (BCC + B2)	6274.1	802.5
	2 Block BCC	6955.3	
	3 W-particle	10,298.3	
AlCrFeNi$W_{0.4}$	1 Matrix (BCC + B2)	6201.9	856.1
	2 Block BCC	6966.9	
	3 W-particle	10,491	

The further addition of W (x = 0.2–0.4) led to the occurrence of strong W particles, causing increment in overall hardness from 669.2 to 856.1 HV. Owing to the increased amount of W addition, more W particles with high hardness formed and precipitated in the matrix and block regions dispersedly, leading to the significantly increased bulk hardness. In addition, solid solution of W in the A2 phase and the appearance of nano-

sized precipitation also positively influence the hardness. However, such contributions are relatively weaker, compared with the W particles precipitation hardening.

In order to obtain more information about the effect of W addition on the mechanical properties of $AlCrFeNiW_x$ (x = 0–0.4) MEAs, compressive tests were carried out in the ambient environment. The representative stress-strain curves are plotted in Figure 5. The mean values of the determined mechanical properties are summarized in Table 6. As shown, the W-free AlCrFeNi alloy in the as-cast state has a yield strength of 1222 MPa, a fracture strength of 2636 MPa and a fracture strain of 41.2%.

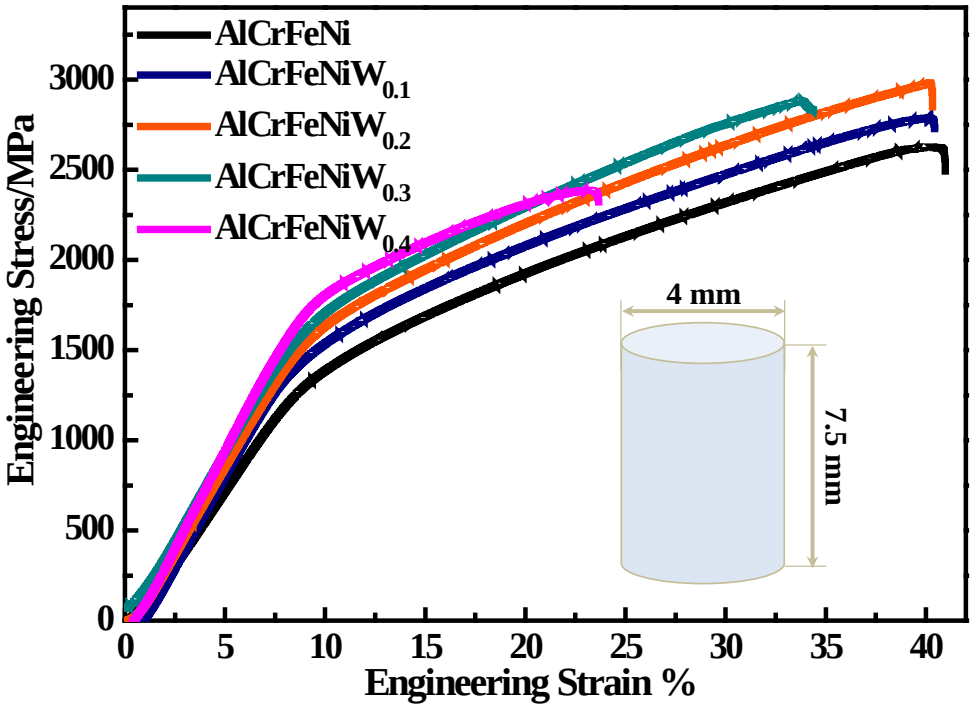

Figure 5. Engineering compressive stress-strain curves of the $AlCrFeNiW_x$ (x = 0–0.4) samples.

Table 6. Mechanical properties of the $AlCrFeNiW_x$ (x = 0–0.4) MEA samples.

Alloys	AlCrFeNi	$AlCrFeNiW_{0.1}$	$AlCrFeNiW_{0.2}$	$AlCrFeNiW_{0.3}$	$AlCrFeNiW_{0.4}$
Yield strength (MPa)	1222	1347	1463	1543	1642
Fracture strength (MPa)	2636	2744	2986	2894	2294
Fracture strain (%)	41.2	40.8	40.7	33.8	23.2

A significant increase in strength and consistently good ductility can be achieved simply by addition of 0.1 and 0.2 molar ratios of W. The yield strength of AlCrFeNiW0.2 was increased to 1463 MPa, and the fracture strength increased to 2986 MPa. The fracture strain is hardly changed (40.7%), compared to that of tungsten-free alloy. The samples with minor tungsten show the high strength and maintain the excellent ductility due to the solid solution of W in the A2 phase and the emergence of nano-sized precipitation. In addition, the appearance of modest small W particles in $AlCrFeNiW_{0.2}$ further benefits the strength of matrix and has no measurable effect on ductility.

With further increasing W, the yield strengths of $AlCrFeNiW_{0.3}$ and $AlCrFeNiW_{0.4}$ samples show a slow rising tendency up to 1543 MPa and 1642 MPa, respectively. On the other hand, a simultaneous decrease in elongation at failure is visible, with the lowest elongation at 23.2% for the sample having W in 0.4 molar ratio. The precipitation of excessive large-sized W-particles is responsible for the reduced ductility of the MEAs.

3.5. Wear Resistance

The dry wear resistance of the MEAs was evaluated under the conditions with or without air flowing involved. For comparison, the resistance of commercial SS316 alloy to dry wear was also evaluated under the same conditions. Figure 6a plots the changes in wear loss versus sliding wear distance for samples under the normal dry condition without the air flow. In general, MEAs with a higher hardness have a better wear resistance than the softer ones. The volume loss is markedly reduced by the W addition with molar ratios of 0.1 and 0.2 and then exhibits a mild decrease with further increasing W content. $AlCrFeNiW_{0.4}$ shows the highest wear resistance among the five MEAs.

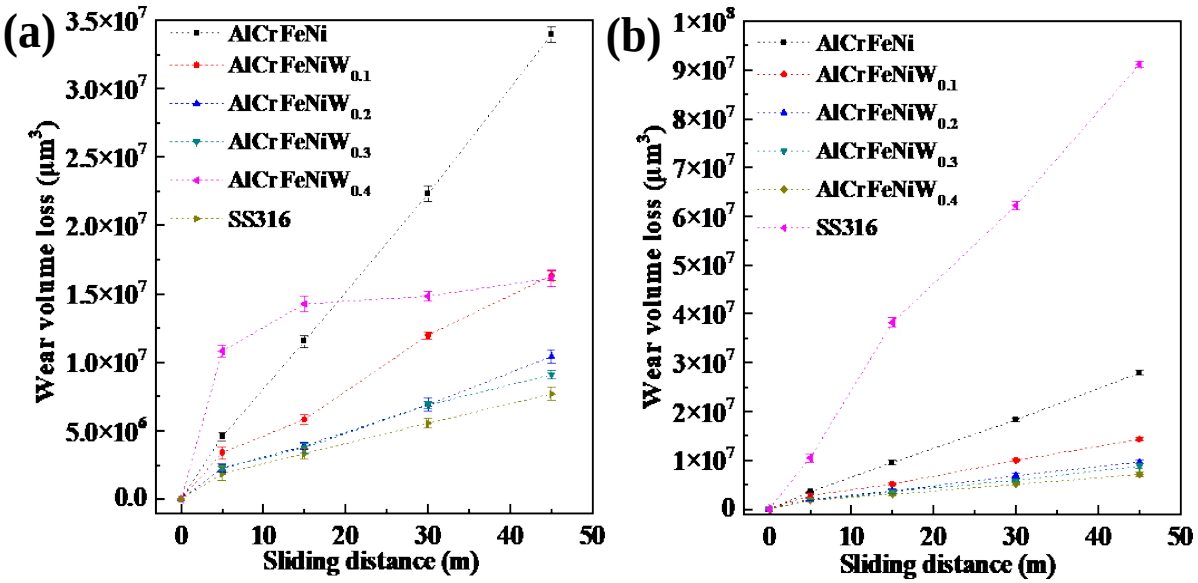

Figure 6. Changes in wear volume loss with respect to the sliding distance for MEAs and SS316 alloys, (**a**) under normal dry sliding condition, and (**b**) with air flow cooling involved.

It is of particular interest to notice that all the MEAs exhibit a linear relationship between wear loss and sliding distance: when sliding distance goes up, wear loss goes up by a fixed amount. However, for the 316SS, the rate of wear loss increase continuously slows down as sliding distance increases, rendering SS316 having the lowest hardness (331 $HV_{0.5}$) performed almost as well as the harder $AlCrFeNiW_{0.1}$ (669.2 $HV_{0.5}$) in the final wear stage. It can be speculated that the wear mechanism would be altered, leading to the change of wear resistance for the alloys, which could be determined via worn surface analysis.

Corresponding worn surfaces of $AlCrFeNiW_x$ and 316SS over a sliding distance of 45 m are illustrated in Figure 7. It is shown that the W-free AlCrFeNi alloy suffered severe abrasive wear, as evidenced by the deep plowing grooves and noticeable patches or debris along the grooves. EDS analysis shows a fair amount of oxygen in the debris, indicating that oxidation occurred during the wear test [58]. The surface was getting smoother and fewer with debris as W was added. Comparison of the worn surface morphology suggests that the ability of MEAs to resist wear is improved with the W content, which is in agreement with the data shown in Figure 6a. Thanks to the solution hardening of A2 phase by W solute as well as the W particles dispersed the MEA matrix which has high thermal stability and high hardness, the wear resistance increased accordingly.

For further understanding of the wear mechanism, worn surface of SS316 is also examined. As shown in Figure 7f, the surface is covered by masses of compact and adherent tribo-oxidation scale, in which the oxygen content is higher than those on MEAs. SS316 is mainly composed of iron and chromium and lack of the other components, such as Al, Ti and Ni, compared with the MEA under study. The heat generated in poorly lubricated friction pairs increases the rate at which iron and chromium oxide form on SS316

steel. As a result, the oxide layer builds up and sustains the wearing force in the ambient environment, leading to marked decrease in wear loss for SS316. The wear mechanism involves oxidative wear and partial abrasion.

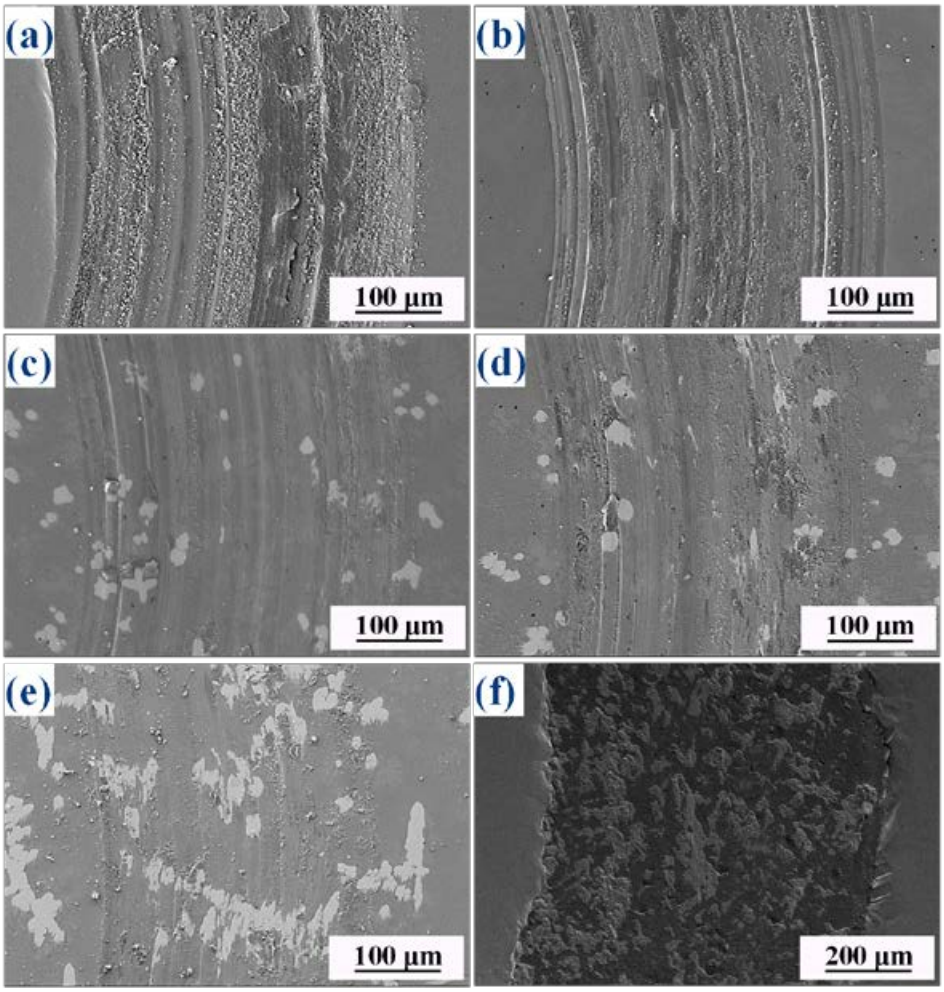

Figure 7. SEM images of worn surfaces for (**a**) AlCrFeNi, (**b**) $AlCrFeNiW_{0.1}$, (**c**) $AlCrFeNiW_{0.2}$, (**d**) $AlCrFeNiW_{0.3}$, (**e**) $AlCrFeNiW_{0.4}$ and (**f**) SS316 alloys after dry sliding over a distance of 45 m.

Figure 6b shows variations in wear loss obtained from another set of tests, which were performed with air flowing to eliminate the effect of frictional heat. The wear resistance of materials is largely dependent on their hardness when frictional oxidation is minimized. As shown, the wear volume loss of 316 SS exhibits a linear increment with the sliding distance, distinctly larger than that of all the MEAs. The transformation of wear performance made by air flow cooling strongly suggests the beneficial role of the oxide scale on 316 SS in resisting wear under normal condition. Since there is a direct relationship between the hardness and wear resistance, a better wear behavior is expected for the harder tungsten-alloyed MEAs. Figure 8 shows the typical worn surface of samples with the air flow cooling. The worn surfaces of AlCrFeNi and $AlCrFeNiW_{0.1}$ are grooved deeply along wear direction, which are similar to the situation without air-flow cooling. Regarding $AlCrFeNiW_x$ (x = 0.2–0.4), the worn surface presents smooth characteristic with a few shallow grooves. The worn surfaces of 316 SS show general wear features of soft materials with ductile deformation. No obvious tribo-oxide was observed on the worn surface for all the alloys.

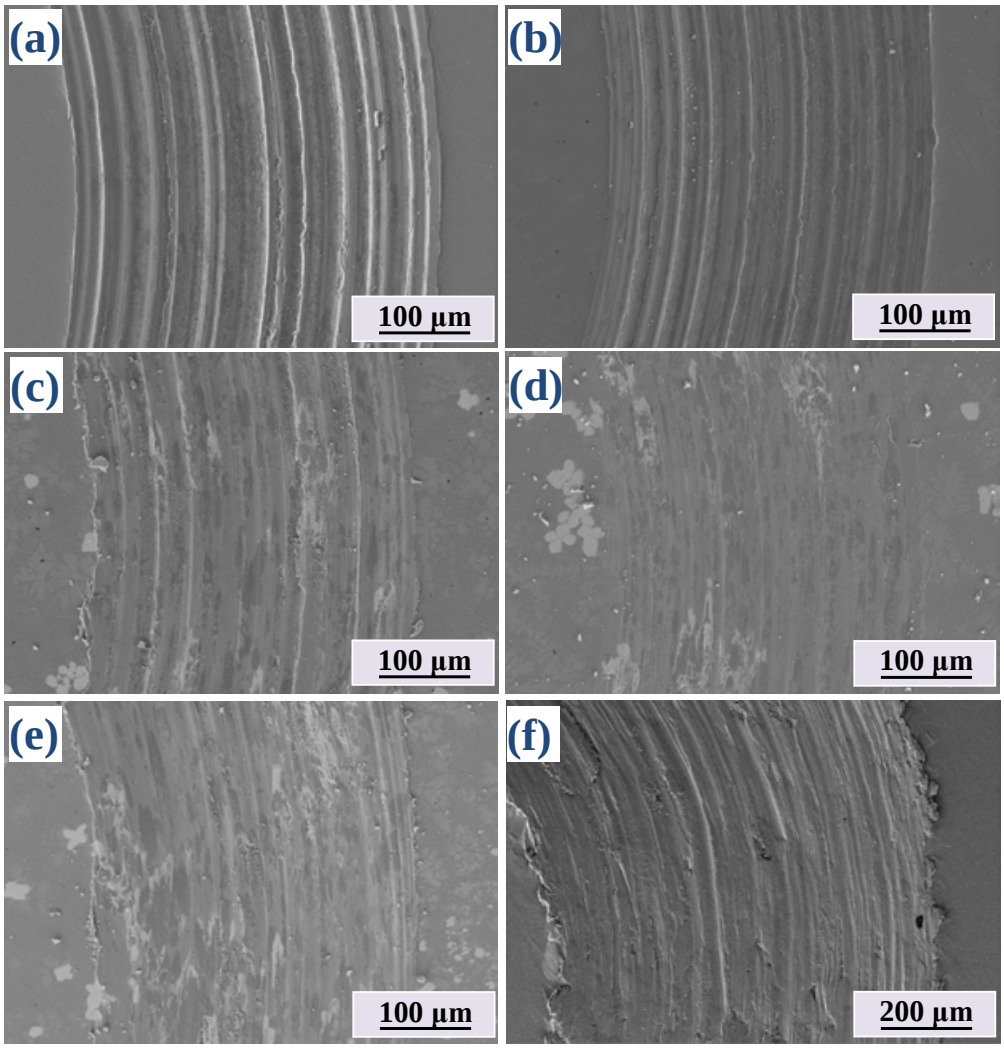

Figure 8. SEM images of worn surfaces for (**a**) AlCrFeNi, (**b**) $AlCrFeNiW_{0.1}$, (**c**) $AlCrFeNiW_{0.2}$, (**d**) $AlCrFeNiW_{0.3}$, (**e**) $AlCrFeNiW_{0.4}$ and (**f**) SS316 alloys after sliding over a distance of 45 m with airflow cooling.

3.6. Corrosion and Corrosive Wear

In order to investigate how W content influences the corrosion performance of the AlCrFeNi alloy, electrochemical corrosion tests were performed on all alloys under study, including $AlCrFeNiW_x$ and SS316 alloys. Figure 9a illustrates the potentiodynamic polarization curves of the alloys in 3.5 wt. % NaCl solution. Thanks to the presence of passive elements of Cr with high concentrations, all the alloys display active-passive transformation on the anodic branch of curves [59]. W addition raises the pitting potential of the MEAs, at which the current increases immediately and the passivation begins to breakdown at localized areas, indicating the improvements in stability and pitting resistance of the passive film with increasing W. When the tungsten content is increased to more than 0.3, the curve shows an instantaneous increase in current on pitting potential and then returns to mild increase as potential continues to increase, which suggests the development or growth of pits on the passive layer or metallic surface are effectively suppressed.

Figure 9b compares the corrosion current and potential of all the alloys obtained from polarization curves. As shown, the corrosion current decreases with increasing W content until 0.3, indicating that the added W positively affects the corrosion resistance of the alloys in the salt solution. Moreover, $AlCrFeNiW_{0.3}$ also shows an increased corrosion resistance in comparison with the corrosion-resistant SS316 alloy, in guidance of the higher corrosion potential and lower corrosion current. It has been reported that the addition of refractory

element W to stainless steel can reduce the corrosion current density and improve the pitting resistance in chloride-containing media [60,61]. The enhancement of the corrosion resistance is primarily attributed to the increased presence of WO_3 in the passivation film, which is well documented the Pourbaix diagram. Tungsten oxide can serve as an efficient inhibitor against pitting corrosion by impeding the binding of anions like Cl^- and Br^-, thus improving the stability of the passivation film in neutral solution [62].

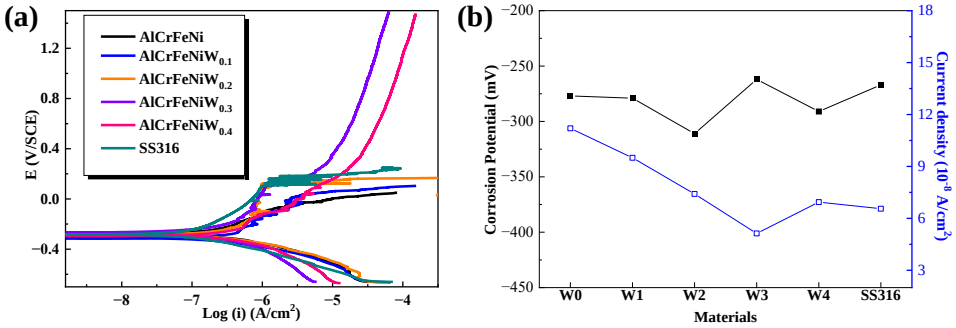

Figure 9. (**a**) Potentialdynamic polarization curves and (**b**) electrochemical parameters for $AlCrFeNiW_x$ and SS316 alloys in 3.5 wt. % NaCl solution.

Resistances of $AlCrFeNiW_x$ and SS316 to corrosive wear in 3.5 wt. % NaCl solution were evaluated for potential tribo-corrosion applications. Obtained results are illustrated in Figure 10, which show a high wear volume loss of the W-free MEA. With the addition of W, a continuous decrease in wear volume loss is achieved. The distinct increase in corrosive wear resistance should be ascribed to the improved hardness and corrosion resistance [58]. In addition, all the MEAs performed much better than SS316, obviously, the volume losses of $AlCrFeNiW_{0.1}$ (8.63×10^6 μm^3) and $AlCrFeNiW_{0.4}$ (6.23×10^6 μm^3) are only about 1/6 and 1/8 volume loss of SS316 (4.87×10^7 μm^3). As demonstrated earlier, the wear loss of 316SS can become nearly equal to that of the $AlCrFeNiW_{0.1}$ under dry wear condition (Figure 3), which is attributed to the formation of thick and adherent tribo-oxide scale on the surface of 316SS. This kind of thick tribo-oxide scale which withstands the wear force is impossible to form in aqueous solution. As a result, the volume loss of 316SS can be markedly increased in the solution because of its lower hardness and less competitive corrosion resistance compared with those of the MEAs.

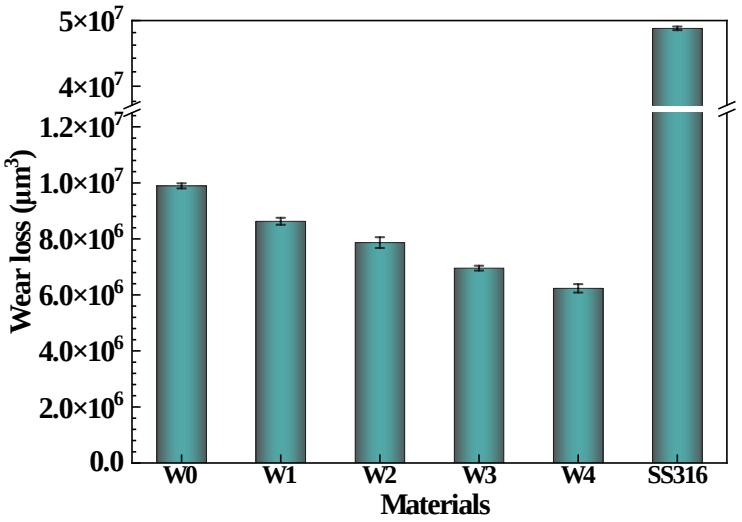

Figure 10. Wear volume losses of $AlCrFeNiW_x$ and SS316 alloys after sliding over a distance of 45 m in 3.5 wt. % NaCl solution.

4. Conclusions

The effects of tungsten addition (x = 0.1, 0.2, 0.3 and 0.4) on microstructure, mechanical properties, wear resistance, corrosion and corrosive wear resistance of A2 + B2 structured AlCrFeNi alloy were investigated. The following conclusions are drawn:

(1) The microstructure of as-cast $AlCrFeNiW_x$ alloys is composed of one disordered Fe-Cr rich BCC phase (A2) and one ordered NiAl rich BCC phase (B2) when x = 0 and 0.1. The W addition mainly stays as a solid solute in A2 BCC phase, strengthening the phase. With 0.2–0.4 molar ratios of W addition, W particles appear in the $AlCrFeNiW_x$ matrix. Besides, the nanoprecipitates are found to be distributed in all the W-containing MEA.

(2) The hardness and strength of AlCrFeNi alloy are obviously enhanced by W addition. The strengthening mechanisms include solid-solution strengthening, nano-sized precipitation strengthening and second phase strengthening. The good ductility of AlCrFeNi is retained with minor W addition ($x \leq 0.2$), while it considerably declines when more W is added due to the precipitation of excessive large-sized W particles.

(3) W addition improves the pitting resistance and passivation property of AlCrFeNi MEA in 3.5 wt. % NaCl solution. It is shown that $AlCrFeNiW_{0.3}$ bears the highest corrosion resistance as demonstrated by the highest E_{corr} and the lowest I_{corr}. Tungsten notably inhibits the wear and corrosive wear of $AlCrFeNiW_x$ alloys. $AlCrFeNiW_{0.4}$ with the highest strength and hardness possesses the lowest wear volume loss under both dry and corrosive wear conditions.

Author Contributions: Conceptualization, M.W. and D.L.; methodology, M.W. and G.D.; validation, M.W., Z.X. and G.D.; formal analysis, M.W. and R.S.; investigation, M.W. and R.S.; resources, D.L., D.C. and W.C.; data curation, M.W. and D.L.; writing—original draft preparation, M.W.; writing—review and editing, D.L., D.C. and W.C.; visualization, M.W.; supervision, D.L. All authors have read and agreed to the published version of the manuscript.

Funding: The authors are grateful for financial support from the Natural Science and Engineering Research Council of Canada (ALLRP 567506-21 Li, ALLRP 561172-20 Li), Alberta Innovates (AB Innovates ADVANCE 202102824 L), Trimay, Mitacs, and High-end Foreign Experts Introduction Project (G2021039004).

Data Availability Statement: The paper is self-containing. For additional information or data, please contact the corresponding author.

Conflicts of Interest: The authors declare no conflict of interest.

References

1. Miracle, D.B.; Senkov, O.N. A critical review of high entropy alloys and related concepts. *Acta Mater.* **2017**, *122*, 448–511. [CrossRef]
2. Tsai, M.-H. Three Strategies for the Design of Advanced High-Entropy Alloys. *Entropy* **2016**, *18*, 252. [CrossRef]
3. Tsai, M.-H.; Yeh, J.-W. High-Entropy Alloys: A Critical Review. *Mater. Res. Lett.* **2014**, *2*, 107–123. [CrossRef]
4. Yeh, J.W.; Chen, S.K.; Lin, S.J.; Gan, J.Y.; Chin, T.S.; Shun, T.T.; Tsau, C.H.; Chang, S.Y. Nanostructured High-Entropy Alloys with Multiple Principal Elements: Novel Alloy Design Concepts and Outcomes. *Adv. Eng. Mater.* **2004**, *6*, 299–303. [CrossRef]
5. Cantor, B.; Chang, I.T.H.; Knight, P.; Vincent, A.J.B. Microstructural development in equiatomic multicomponent alloys. *Mater. Sci. Eng. A* **2004**, *375–377*, 213–218. [CrossRef]
6. Liu, Y.; Zhang, F.; Huang, Z.; Zhou, Q.; Ren, Y.; Du, Y.; Wang, H. Mechanical and dry sliding tribological properties of CoCrNiNbx medium-entropy alloys at room temperature. *Tribol. Int.* **2021**, *163*, 107160. [CrossRef]
7. Owen, L.R.; Jones, N.G. Lattice distortions in high-entropy alloys. *J. Mater. Res.* **2018**, *33*, 2954–2969. [CrossRef]
8. Peighambardoust, N.S.; Alamdari, A.A.; Unal, U.; Motallebzadeh, A. In Vitro biocompatibility evaluation of $Ti_{1.5}ZrTa_{0.5}Nb_{0.5}Hf_{0.5}$ refractory high-entropy alloy film for orthopedic implants: Microstructural, mechanical properties and corrosion behavior. *J. Alloys Compd.* **2021**, *883*, 160786. [CrossRef]
9. Qiu, Y.; Hu, Y.J.; Taylor, A.; Styles, M.J.; Marceau, R.K.W.; Ceguerra, A.V.; Gibson, M.A.; Liu, Z.K.; Fraser, H.L.; Birbilis, N. A lightweight single-phase AlTiVCr compositionally complex alloy. *Acta Mater.* **2017**, *123*, 115–124. [CrossRef]
10. Sun, S.J.; Tian, Y.Z.; Lin, H.R.; Lu, S.; Yang, H.J.; Zhang, Z.F. Modulating the prestrain history to optimize strength and ductility in CoCrFeMnNi high-entropy alloy. *Scr. Mater.* **2019**, *163*, 111–115. [CrossRef]

11. Wang, Z.; Baker, I.; Guo, W.; Poplawsky, J.D. The effect of carbon on the microstructures, mechanical properties, and deformation mechanisms of thermo-mechanically treated $Fe_{40.4}Ni_{11.3}Mn_{34.8}Al_{7.5}Cr_6$ high entropy alloys. *Acta Mater.* **2017**, *126*, 346–360. [CrossRef]
12. Ye, F.; Jiao, Z.; Yan, S.; Guo, L.; Feng, L.; Yu, J. Microbeam plasma arc remanufacturing: Effects of Al on microstructure, wear resistance, corrosion resistance and high temperature oxidation resistance of $Al_xCoCrFeMnNi$ high-entropy alloy cladding layer. *Vacuum* **2020**, *174*, 109178. [CrossRef]
13. Zhang, Z.; Armstrong, D.E.J.; Grant, P.S. The effects of irradiation on CrMnFeCoNi high-entropy alloy and its derivatives. *Prog. Mater. Sci.* **2022**, *123*, 100807. [CrossRef]
14. Liu, B.; Wang, J.; Liu, Y.; Fang, Q.; Wu, Y.; Chen, S.; Liu, C.T. Microstructure and mechanical properties of equimolar FeCoCrNi high entropy alloy prepared via powder extrusion. *Intermetallics* **2016**, *75*, 25–30. [CrossRef]
15. Tsau, C.-H.; Lin, S.-X.; Fang, C.-H. Microstructures and corrosion behaviors of FeCoNi and CrFeCoNi equimolar alloys. *Mater. Chem. Phys.* **2017**, *186*, 534–540. [CrossRef]
16. Chen, S.; Oh, H.S.; Gludovatz, B.; Kim, S.J.; Park, E.S.; Zhang, Z.; Ritchie, R.O.; Yu, Q. Real-time observations of TRIP-induced ultrahigh strain hardening in a dual-phase CrMnFeCoNi high-entropy alloy. *Nat. Commun.* **2020**, *11*, 826. [CrossRef] [PubMed]
17. Cantor, B. Multicomponent high-entropy Cantor alloys. *Prog. Mater. Sci.* **2021**, *120*, 100754. [CrossRef]
18. Zeng, Z.; Xiang, M.; Zhang, D.; Shi, J.; Wang, W.; Tang, X.; Tang, W.; Wang, Y.; Ma, X.; Chen, Z.; et al. Mechanical properties of Cantor alloys driven by additional elements: A review. *J. Mater. Res. Technol.* **2021**, *15*, 1920–1934. [CrossRef]
19. Bhalla, S.; Melnekoff, D.T.; Aleman, A.; Leshchenko, V.; Restrepo, P.; Keats, J.; Onel, K.; Sawyer, J.R.; Madduri, D.; Richter, J.; et al. Patient similarity network of newly diagnosed multiple myeloma identifies patient subgroups with distinct genetic features and clinical implications. *Sci. Adv.* **2021**, *7*, eabg9551. [CrossRef]
20. Liu, W.H.; Yang, T.; Liu, C.T. Precipitation hardening in CoCrFeNi-based high entropy alloys. *Mater. Chem. Phys.* **2018**, *210*, 2–11. [CrossRef]
21. Salishchev, G.; Tikhonovsky, M.; Shaysultanov, D.G.; Stepanov, N.; Kuznetsov, A.V.; Kolodiy, I.; Tortika, A.S.; Senkov, O. Effect of Mn and V on structure and mechanical properties of high-entropy alloys based on CoCrFeNi system. *J. Alloys Compd.* **2014**, *591*, 11–21. [CrossRef]
22. Shun, T.-T.; Chang, L.-Y.; Shiu, M.-H. Microstructures and mechanical properties of multiprincipal component $CoCrFeNiTi_x$ alloys. *Mater. Sci. Eng. A* **2012**, *556*, 170–174. [CrossRef]
23. Huo, W.; Zhou, H.; Fang, F.; Xie, Z.; Jiang, J. Microstructure and mechanical properties of $CoCrFeNiZr_x$ eutectic high-entropy alloys. *Mater. Des.* **2017**, *134*, 226–233. [CrossRef]
24. Jiang, H.; Han, K.; Qiao, D.; Lu, Y.; Cao, Z.; Li, T. Effects of Ta addition on the microstructures and mechanical properties of CoCrFeNi high entropy alloy. *Mater. Chem. Phys.* **2018**, *210*, 43–48. [CrossRef]
25. Zhang, L.J.; Zhang, M.D.; Zhou, Z.; Fan, J.T.; Cui, P.; Yu, P.F.; Jing, Q.; Ma, M.Z.; Liaw, P.K.; Li, G.; et al. Effects of rare-earth element, Y, additions on the microstructure and mechanical properties of CoCrFeNi high entropy alloy. *Mater. Sci. Eng. A* **2018**, *725*, 437–446. [CrossRef]
26. Niu, Z.; Xu, J.; Wang, T.; Wang, N.; Han, Z.; Wang, Y. Microstructure, mechanical properties and corrosion resistance of CoCrFeNiW*x* (*x* = 0, 0.2, 0.5) high entropy alloys. *Intermetallics* **2019**, *112*, 106550. [CrossRef]
27. Ma, H.; Shao, Y.; Shek, C.H. CoCuFeNi high entropy alloy reinforced by in-situ W particles. *Mater. Sci. Eng. A* **2020**, *797*, 140218. [CrossRef]
28. Ma, H.; Shek, C.H. Effects of Hf on the microstructure and mechanical properties of CoCrFeNi high entropy alloy. *J. Alloys Compd.* **2020**, *827*, 154159. [CrossRef]
29. Shao, Y.; Ma, H.; Wang, Y. Effect of Mo Addition on The Microstructure and Mechanical Properties of CoCuFeNi High Entropy Alloy. *Metals* **2020**, *10*, 1017. [CrossRef]
30. Chuang, M.-H.; Tsai, M.; Wang, W.-R.; Lin, S.-J.; Yeh, J.-W. Microstructure and wear behavior of $Al_xCo_{1.5}CrFeNi_{1.5}Ti_y$ high-entropy alloys. *Acta Mater.* **2011**, *59*, 6308–6317. [CrossRef]
31. Wang, S.; Chen, L.; Li, Q.; Wang, S.; Wu, M.; Yang, S.; Xiang, D. Effects of Al or Mo Addition on Microstructure and Mechanical Properties of Fe-Rich Nonequiatomic FeCrCoMnNi High-Entropy Alloy. *Metals* **2022**, *12*, 191. [CrossRef]
32. Ma, Y.; Jiang, B.; Li, C.; Wang, Q.; Dong, C.; Liaw, P.K.; Xu, F.; Sun, L. The BCC/B2 Morphologies in Al_xNiCoFeCr High-Entropy Alloys. *Metals* **2017**, *7*, 57. [CrossRef]
33. Coutinho, Y.A.; Kunwar, A.; Moelans, N. Phase-field approach to simulate BCC-B_2 phase separation in the $Al_nCrFe_2Ni_2$ medium-entropy alloy. *J. Mater. Sci.* **2022**, *57*, 10600–10612. [CrossRef]
34. Jin, D.-M.; Wang, Z.-H.; Li, J.-F.; Niu, B.; Wang, Q. Formation of coherent BCC/B_2 microstructure and mechanical properties of Al–Ti–Zr–Nb–Ta–Cr/Mo light-weight refractory high-entropy alloys. *Rare Met.* **2022**, *41*, 2886–2893. [CrossRef]
35. Wang, H.; Zhang, W.; Gao, P.; Xiang, Q.; Qu, Y.; Cheng, J.; Ren, Y.; Yu, B.; Qiu, K. Al_xCrFeNi medium entropy alloys with high damping capacity. *J. Alloys Compd.* **2021**, *876*, 159991. [CrossRef]
36. Jiao, W.; Li, T.; Chang, X.; Lu, Y.; Yin, G.; Cao, Z.; Li, T. A novel Co-free $Al_{0.75}$CrFeNi eutectic high entropy alloy with superior mechanical properties. *J. Alloys Compd.* **2022**, *902*, 163814. [CrossRef]
37. Jiang, Z.; Chen, W.; Xia, Z.; Xiong, W.; Fu, Z. Influence of synthesis method on microstructure and mechanical behavior of Co-free AlCrFeNi medium-entropy alloy. *Intermetallics* **2019**, *108*, 45–54. [CrossRef]

38. Wu, M.; Yuan, J.; Diao, G.; Li, D. Achieving a Combination of Higher Strength and Higher Ductility for Enhanced Wear Resistance of $AlCrFeNiTi_{0.5}$ High-Entropy Alloy by Mo Addition. *Metals* **2022**, *12*, 1910. [CrossRef]
39. Ossiansson, M.; Gupta, M.; Löbel, M.; Lindner, T.; Lampke, T.; Joshi, S. Assessment of CrFeCoNi and AlCrFeCoNi High-Entropy Alloys as Bond Coats for Thermal Barrier Coatings. *J. Therm. Spray Technol.* **2022**, *31*, 1404–1422. [CrossRef]
40. Günen, A.; Lindner, T.; Karakaş, M.S.; Kanca, E.; Töberling, G.; Vogt, S.; Gök, M.S.; Lampke, T. Effect of the boriding environment on the wear response of laser-clad AlCoCrFeNi high entropy alloy coatings. *Surf. Coat. Technol.* **2022**, *447*, 128830. [CrossRef]
41. Ghadami, F.; Ghadami, S.; Davoudabadi, M.A. Sliding wear behavior of the nanoceria-doped AlCrFeCoNi high-entropy alloy coatings deposited by air plasma spraying technique. *J. Therm. Spray Technol.* **2022**, *31*, 1263–1275. [CrossRef]
42. Wu, M.; Chen, K.; Xu, Z.; Li, D.Y. Effect of Ti addition on the sliding wear behavior of AlCrFeCoNi high-entropy alloy. *Wear* **2020**, *462*, 203493. [CrossRef]
43. Terajima, T.; Nakata, K.; Kimura, H.; Inoue, A. Development of W-Reinforced Zr-Based Metallic Glass. *J. Jpn. Inst. Met. Mater.* **2010**, *74*, 85–88. [CrossRef]
44. Bauri, R.; Yadav, D.; Shyam Kumar, C.N.; Balaji, B. Tungsten particle reinforced Al 5083 composite with high strength and ductility. *Mater. Sci. Eng. A* **2015**, *620*, 67–75. [CrossRef]
45. Mazilkin, A.; Abramova, M.M.; Enikeev, N.A.; Lomakin, I.V.; Valiev, R.Z.; Ivanisenko, Y.; Kübel, C.; Etienne, A.; Sauvage, X.; Radiguet, B. The effect of tungsten on microstructure and mechanical performance of an ultrafine Fe-Cr steel. *Mater. Lett.* **2018**, *227*, 292–295. [CrossRef]
46. Jiang, H.; Jiang, L.; Han, K.; Lu, Y.; Wang, T.; Cao, Z.; Lu, Y. Effects of Tungsten on Microstructure and Mechanical Properties of $CrFeNiV_{0.5}W_x$ and $CrFeNi_2V_{0.5}W_x$ High-Entropy Alloys. *J. Mater. Eng. Perform.* **2015**, *24*, 4594–4600. [CrossRef]
47. Chang, R.; Fang, W.; Bai, X.; Xia, C.; Zhang, X.; Yu, H.; Liu, B.; Yin, F. Effects of tungsten additions on the microstructure and mechanical properties of CoCrNi medium entropy alloys. *J. Alloys Compd.* **2019**, *790*, 732–743. [CrossRef]
48. Soni, V.K.; Sanyal, S.; Sinha, S.K. Influence of tungsten on microstructure evolution and mechanical properties of selected novel $FeCoCrMnW_x$ high entropy alloys. *Intermetallics* **2021**, *132*, 107161. [CrossRef]
49. Zhang, Y.; Zhou, Y.J.; Lin, J.P.; Chen, G.L.; Liaw, P.K. Solid-Solution Phase Formation Rules for Multi-component Alloys. *Adv. Eng. Mater.* **2008**, *10*, 534–538. [CrossRef]
50. Guo, S.; Ng, C.; Lu, J.; Liu, C. Effect of valence electron concentration on stability of fcc or bcc phase in high entropy alloys. *J. Appl. Phys.* **2011**, *109*, 103505. [CrossRef]
51. Yang, X.; Zhang, Y. Prediction of high-entropy stabilized solid-solution in multi-component alloys. *Mater. Chem. Phys.* **2012**, *132*, 233–238. [CrossRef]
52. Singh, A.; Kumar, N.; Dwivedi, A.; Subramaniam, A. A geometrical parameter for the formation of disordered solid solutions in multi-component alloys. *Intermetallics* **2014**, *53*, 112–119. [CrossRef]
53. Wang, Z.; Huang, Y.; Yang, Y.; Wang, J.; Liu, C.T. Atomic-size effect and solid solubility of multicomponent alloys. *Scr. Mater.* **2015**, *94*, 28–31. [CrossRef]
54. Rao, Z.; Dutta, B.; Körmann, F.; Lu, W.; Zhou, X.; Liu, C.; da Silva, A.K.; Wiedwald, U.; Spasova, M.; Farle, M.; et al. Beyond Solid Solution High-Entropy Alloys: Tailoring Magnetic Properties via Spinodal Decomposition. *Adv. Funct. Mater.* **2021**, *31*, 2007668. [CrossRef]
55. Findik, F. Modulated (Spinodal) Alloys. *Period. Eng. Nat. Sci. (PEN)* **2013**, *1*, 1. [CrossRef]
56. Shim, S.H.; Pouraliakbar, H.; Lee, B.J.; Kim, Y.K.; Rizi, M.S.; Hong, S.I. Strengthening and deformation behavior of as-cast CoCrCu1.5MnNi high entropy alloy with micro-/nanoscale precipitation. *Mater. Sci. Eng. A* **2022**, *853*, 143729. [CrossRef]
57. Saboktakin Rizi, M.; Minouei, H.; Lee, B.J.; Toroghinejad, M.R.; Hong, S.I. Effects of carbon and molybdenum on the nanostructural evolution and strength/ductility trade-off in $Fe_{40}Mn_{40}Co_{10}Cr_{10}$ high-entropy alloys. *J. Alloys Compd.* **2022**, *911*, 165108. [CrossRef]
58. Wang, S.D.; Wu, M.Y.; Xu, D.K.; Han, E.-h. Improving corrosive wear resistance of Mg-Zn-Y-Zr alloys through heat treatment. *J. Magnes. Alloy.* **2021**. [CrossRef]
59. Wang, S.D.; Xu, D.K.; Wang, B.J.; Sheng, L.Y.; Qiao, Y.X.; Han, E.-H.; Dong, C. Influence of phase dissolution and hydrogen absorption on the stress corrosion cracking behavior of Mg-7%Gd-5%Y-1%Nd-0.5%Zr alloy in 3.5 wt.% NaCl solution. *Corros. Sci.* **2018**, *142*, 185–200. [CrossRef]
60. Brigham, R.J. Pitting of Molybdenum Bearing Austenitic Stainless Steel. *Corrosion* **2013**, *28*, 177–179. [CrossRef]
61. Zhang, X.; Lai, L.; Xiao, S.; Zhang, H.; Zhang, F.; Li, N.; Guo, S. Effect of W on the thermal stability, mechanical properties and corrosion resistance of Fe-based bulk metallic glass. *Intermetallics* **2022**, *143*, 107485. [CrossRef]
62. Kumar, D.; Maulik, O.; Sharma, V.K.; Prasad, Y.V.S.S.; Kumar, V. Understanding the Effect of Tungsten on Corrosion Behavior of $AlCuCrFeMnW_x$ High-Entropy Alloys in 3.5 wt.% NaCl Solution. *J. Mater. Eng. Perform.* **2018**, *27*, 4481–4488. [CrossRef]